Zhu C, Seo J, Mittal R. Computational Modeling and Analysis of Murmurs Generated by Modeled Aortic Stenoses. ASME. J Biomech Eng. 2019;141(4): 041007-041007-12. doi:10.1115/1.4042765.

Computational Modeling and Analysis of Murmurs Generated by Modeled Aortic Stenoses

Chi Zhu
Graduate Student
Department of Mechanical Engineering,
Johns Hopkins University,
3400 N. Charles Street, Baltimore, MD 21218, USA
czhu19@jhu.edu

Jung-Hee Seo
Associate Research Professor
Department of Mechanical Engineering,
Johns Hopkins University,
3400 N. Charles Street, Baltimore, MD 21218, USA
jhseo@jhu.edu

Rajat Mittal[1]
Professor
Department of Mechanical Engineering,
Johns Hopkins University,
3400 N. Charles Street, Baltimore, MD 21218, USA
mittal@jhu.edu

ABSTRACT

In this study, coupled hemodynamic-acoustic simulations are employed to study the generation and propagation of murmurs associated with aortic stenoses where the aorta with a stenosed aortic valve is modeled as a curved pipe with a constriction near the inlet. The hemodynamics of the post-stenotic flow is investigated in detail in our previous numerical study[1]*. The temporal history of the pressure on the aortic lumen is recorded during the hemodynamic study and used as the murmur source in the acoustic simulations. The thorax is modeled as an elliptic cylinder and the thoracic tissue is assumed to be homogeneous, linear and viscoelastic. A previously developed high-order numerical method that is capable*

[1] Corresponding author.

of dealing with immersed bodies is applied in the acoustic simulations. To mimic the clinical practice of auscultation, the sound signals from the epidermal surface are collected. The simulations show that the source of the aortic stenosis murmur is located at the proximal end of the aortic arch and that the sound intensity pattern on the epidermal surface can predict the source location of the murmurs reasonably well. Spectral analysis of the murmur reveals the disconnect between the break frequency obtained from the flow and from the murmur signal. Finally, it is also demonstrated that the source locations can also be predicted by solving an inverse problem using the free-space Green's function. The implications of these results for cardiac auscultation are discussed.

1. INTRODUCTION

Auscultation with a stethoscope has long been one of the primary modalities for screening, diagnosing and monitoring a variety of cardiovascular conditions[2]. One common condition is the vascular stenosis which is known to generate murmurs (or bruits) [2] that contain important diagnostic information and can be detected through stethoscope on the skin surface. Compared with other diagnostic modalities, such as CT, MRI and echocardiography, auscultation has the advantage of being low-cost, noninvasive and complication-free. Researchers have been striving to convert auscultation into a quantitative diagnostic tool since 1970s [3–7]. Moreover, due to the recent development of ultra-sensitive, low-cost, compact acoustic sensors, advanced signal processing tools and powerful portable computers, researchers have also been exploring the possibility of developing automated auscultation systems[8, 9]. Such systems would reduce the subjectivity associated with human hearing acuity and training, making it suitable for rapid mass diagnostic screening, longitudinal (tracking over time) at-home monitoring of patient health, and field operations in areas with

limited medical access. However, this requires a much better understanding of the causal mechanism(s) between specific medical condition and the associated murmurs as well as the propagation (travelling through the tissue) characteristics of these murmurs.

The understanding of the causal mechanism(s) can be facilitated by studying the coupled physics of hemodynamics and elastic wave propagation that are implicated in the generation and propagation of the murmurs. The generation of stenosis related murmurs has been studied extensively [1,10-13], where it was concluded that the murmurs were generated by the abnormal pressure fluctuations at the vessel wall. Moreover, the source location, where the most intense pressure fluctuations were observed, was found not at the site of the stenosis but further downstream.

The propagation of the elastic waves inside the body, which is the focus of this paper, has also been studied by many researchers[4, 10, 11, 14–16]. Previous studies focused mainly on two aspects of the murmurs. The first was the spectral characteristics of the signal, which served as the “fingerprints” of the related medical condition. Fredberg [14] used analytical solutions to predict how the propagation inside the tissue would alter the source spectrum (signal distribution according to frequency). He concluded that the change in spectrum measured at the skin surface was not a consequence of volume absorption by the tissue, but due to the superimposition of pressure waves generated at different locations along the axial direction of the stenosed vessel. It is noted that shear waves were not included in the calculation. Duncan et al. [4] conducted in-vivo measurements of murmurs from patients with carotid stenosis and identified the break frequency (f_b), a critical value around which the slope of the

spectrum changed dramatically. They were able to relate the break frequency to the severity of the stenosis through $D_j = U/f_b$, where D_j was the diameter of the lumen at the stenosis, and U was the peak systolic velocity at the healthy part of the artery. The break frequency was also observed in the numerical study by Seo & Mittal [10].

The second focus of many studies has been on localization of the murmur source. Since the source location usually lies in the vicinity of the stenosis, correctly identifying the source location only using the murmurs can provide valuable diagnostic information. Owsley & Hull[15] built an experimental set-up where a straight tube with a constriction was incorporated within a tissue-mimicking gelatin, and a sensor array was used to measure the acoustic signals at the surface. Then, a nearfield beamforming process was employed to image the shear wave energy distribution inside the gelatin to noninvasively determine the source location. They found that the source could be accurately located when there was no obstacle inside, but when dog ribs were included in the gelatin, the accuracy varied based on the frequency band. Cooper et al. [16] applied finite element analysis to study the wave propagation inside a two-dimensional cross-section of a physiologically accurate human thorax model. In order to obtain the transfer function between the murmurs and the source signal, they conducted a series of simulations to study the surface signals generated by point sources placed at different locations of the thorax. They claimed that the obtained transfer function could be useful in separating multiple co-existing acoustic sources. It should be noted again that only compression waves were included in the study.

Despite the aforementioned studies, there is a disconnect between the studies of murmur generation and of murmur propagation, since these are mostly studied as separate problems. For instance, many studies of the post-stenotic flow identified a critical frequency in the spectrum of the wall pressure fluctuations [12, 17]. This critical frequency has the same definition as the break frequency in the murmur signal. However, the relationship between the hemodynamic break frequency of the flow and the acoustic break frequency of the murmurs is not understood.

Moreover, in some studies of the murmur propagation inside the thorax, an artificial point source was used [18–20], but this ignored the reality that the source could be distributed over a relatively large area. In experimental studies where the murmurs were generated from modeled stenoses [15, 21], access to flow information was greatly restricted due to the inherent limitations of the experiments, making it difficult to draw the connections between the post-stenotic flow and the murmurs. Thus, the current study will adopt a coupled hemodynamic-acoustic (termed "hemoacoustic") computational approach [22].

In the present study, we focus on systolic murmurs due to aortic stenosis, which refers to the abnormal narrowing at the aortic valve region due to the incomplete opening of the leaflets. Aortic stenosis is the most common valvular disease and is known to create systolic murmurs [23]. The current study is motivated by the potential of using automated cardiac auscultation systems for at-home monitoring of patients with this condition. Our team has developed a wearable acoustic sensor array that is designed for such applications[8, 24]. Such a system could enable longitudinal tracking

of the progression of the condition and enable the optimization of the treatment. However, to develop appropriate signal analysis algorithms that can identify and localize the murmurs associated with diseases such as the aortic stenosis, a better understanding of the generation and propagation of these murmurs is required. Providing these insights is the primary motivation for the current study.

In this study, the generation and propagation of murmurs associated with aortic stenosis are studied in a coupled fashion using numerical simulations from first principles. First, hemodynamic simulations are performed to study the post-stenotic flows. The key flow patterns, source locations as well as the characteristic frequencies of the source are identified [1]. Then, the flow information is used as the input in the acoustic simulations to study the propagation of the elastic waves inside the modeled thorax and the characteristics of the resulting murmurs measured on the epidermal surface. Another important feature of the current study is the inclusion of shear waves in murmur propagation, which have been excluded in many previous studies[10,14,16]. Zhu et al. [11] already demonstrated through a classic vector decomposition that the shear waves had a significant impact on the spectra of the murmurs and acoustic energy distribution on the epidermal surface, and inclusion of this effect in our study should lead to more realistic modeling of murmur propagation.

The paper is organized as follows. First, the model employed in the study is introduced in Section 2. Some key findings of the hemodynamic simulations are summarized in Section 3.1 and the results from the acoustic simulations are presented afterwards. Then, a discussion of a free space Green's function based source localization

method is provided in Section 3.4. Finally, some concluding remarks as well as the implications of the current study to the cardiac auscultation are presented in Section 4.

2. MODEL CONFIGURATION

Fig. 1 shows the geometry adopted in the current study. As shown in Fig. 1a, the aorta is modeled as a curved pipe with 180^o turn representing ascending and descending parts of the aorta. A smooth, axisymmetric occlusion is prescribed near the inlet to serve as a stenosis caused by the incomplete opening of the aortic valve. The profile of the stenosis can be found in Refs. [1, 22]. The degree/severity of the stenosis is quantified using the area stenosis ratio (*AS*) and is defined as the percentage of area that is blocked due to the stenosis and can be calculated by $AS = 1 - \left(D_j/D\right)^2$, where D is the diameter of the healthy part of the aorta and D_j is the minimal diameter (also the jet diameter) at the stenosed section. Using continuity, the mean velocity at the stenosis (jet velocity) is $V_j = V_{in}/(1 - AS)$, and V_{in} is the inlet velocity. The flow in the stenosed aorta is governed by the incompressible Naiver-Stokes equations.

The thorax is modeled as an elliptic cylinder in this study, as shown in Fig. 1b. Dimensions of the geometry are provided in Fig. 1c. In reality, the human thorax is highly inhomogeneous and consists of bones, lungs, muscles and other tissues. However, to simplify the problem, the thorax is treated as a homogeneous, linear material here, and the viscoelastic behavior of the tissue is described by the Kelvin-Voigt model. The resulting governing equations for elastic wave propagation are

$$\rho_s \frac{\partial u_i}{\partial t} + \frac{\partial p_{ij}}{\partial x_j} = \eta \frac{\partial}{\partial x_j}\left(\frac{\partial u_i}{\partial x_j} + \frac{\partial u_j}{\partial x_i}\right),$$
$$\frac{\partial p_{ij}}{\partial t} + \lambda \frac{\partial u_k}{\partial x_k}\delta_{ij} + \mu\left(\frac{\partial u_i}{\partial x_j} + \frac{\partial u_j}{\partial x_i}\right) = 0, \quad (1)$$

where the indices i and j range from 1 to 3. u_i and p_{ij} are the velocity vector and the stress tensor in the thorax. ρ_s, η, λ, and μ are the density, viscosity, first and second Lame constants of the material, respectively. δ_{ij} is the Kronecker delta function, and it has value 1 when $i = j$ and value 0 when $i \neq j$. This linear material model is considered valid in the current problem due to the very small $O(10^{-7})m$ displacement caused by the elastic waves. The same material model is also employed in the earlier study [22].

Previous studies of the fluid dynamics and acoustics associated with heart murmurs [10, 25, 26] have concluded that the generation of a murmurs is closely associated with the pressure force on the wall of the blood vessel. Seo et al. [22] demonstrated that the elastic wave velocity at the blood-tissue interface was about $O(10^{-3})$ of the blood velocity scale. This large separation of velocity scales enables us to employ the one-way coupled approach develop in Ref [22] to solve this hemoacoustic problem. First, the flow inside a modeled aorta with stenosis (Fig. 1a) is simulated with a sharp-interface immersed boundary flow solver [27–29]. Since this study aims to delineate the connections between the abnormal fluid behaviors and the murmur signals, a uniform steady inflow (V_{in}) is prescribed at the inlet of the aorta to avoid the extra complications and parameters introduced by pulsatility. The zero-pressure-gradient and zero-velocity-gradient boundary condition is applied at the outlet. The temporal history of the wall pressure is recorded during the hemodynamic simulations

and is subsequently applied in the acoustic simulations as the boundary condition at the vessel-tissue interface.

In the hemodynamic simulations, V_{in} and D are 0.25*m/s* and 2.5*cm,* respectively. Along with a kinematic viscosity (ν) of $3.125\times10^{-6} m^2/s$, these parameters result in a Reynolds number $(Re = V_{in}D/\nu)$ of 2000, which matches the Reynolds number employed in other experimental studies [30–32]. Three different cases with *AS*=50%, 62.5% and 75% are studied to reveal the effect of the severity on the characteristics of murmurs. They correspond to valve opening areas of 2.45cm^2, 1.84cm^2 and 1.23cm^2, respectively. More details about the hemodynamic simulations can be found in Ref. [1].

In the acoustic simulations, the material properties of the thorax are modeled after a widely-used tissue mimicking material, EcoFlex-10. The density of the material is $1040 kg/m^3$. The shear wave speed (c_s) and compression wave speed (c_p) are 4.2*m/s* and 1000*m/s*, respectively, and the viscosity of the material is $14 Pa\cdot s$. It is noted that the compression wave Mach number (V_{in}/c_p) of the problem is 2.5×10^{-4}. This large separation of velocity scales imposes a very strict CFL condition based time-step size constraint on the acoustic simulations. In order to simulate the problem with reasonable computational cost, the compression wave speed in this study is reduced by one order of magnitude to 100m/s while the shear wave speed is kept unchanged. The effect of this practice is rigorously tested in Ref. [22], and it shows little effect on the wave propagation since the wave length of the compression wave with decreased speed is still significantly longer than the characteristic length of the thorax at the frequency range of interest ($f < 1000Hz$).

The acoustic simulations are conducted with the high-order, immersed boundary based, finite-difference solver developed by Seo et al. [22]. The computational domain in the acoustic simulations is discretized by a uniform, isotropic grid with 190, 360 and 220 (~15 million) grid points along the minor axis, major axis and z direction, respectively. The grid spacing is about 0.027D, and a shear wave at 400Hz is resolved by around 16 points/wavelength with this grid spacing, which is well above the 8 points/wavelength recommended for this high-order solver [22]. The energy transfer and annihilating non-reflecting boundary condition [33] is adopted at the top and bottom of the elliptical cylinder to significantly reduce the reflection of the elastic waves. The buffer zone is set to be 20 grid points on each end. Given the drastically different acoustic impedances between air and tissue, a traction-free boundary condition is applied on the side of the modeled thorax to model the air-tissue interface. It takes 96 hours of wall time to obtain 1.2s of acoustic signals on TACC-Stampede1 supercomputer using 600 cores. More details regarding the numerical methods employed in the hemoacoustic simulations as well as validation against experiments can be found in Ref. [22].

3. RESULTS

In this section, the results from the hemodynamic study are summarized first to provide the necessary information for the following discussion of acoustic simulations. Subsequently, the acoustic simulations for three cases with different degrees of stenosis (50%, 62.5% and 75%) are presented. Results from the 75% case are presented in detail

first, and the other two cases are discussed in comparison to the 75% case. The following characteristic scales are used to non-dimensionalize the results unless otherwise stated: velocity scale, c_p; length scale, D; time scale, D/c_p; pressure/stress scale, $\rho_s c_p^2$. The Strouhal number is defined as $St = fD/c_p$. Moreover, since the problem is symmetric with regard to the frontal plane, results from the anterior and posterior surface are ensemble averaged when appropriate.

3.1 Hemodynamics

The details of the computed hemodynamics can be found in Ref. [1], but some salient results are presented here to facilitate the discussion. The post-stenotic flows for the three cases studied here share very similar behaviors and we therefore present most results for the 75% stenosis case. Fig. 2 shows the instantaneous azimuthal vorticity field on the frontal plane and the streamwise vorticity on one cross-section for this case. The definition of the azimuthal and streamwise directions can be found in Fig. 1a. From the azimuthal vorticity on the frontal plane we can observe a jet forming at the stenosis; as the jet propagates downstream, it impinges on the wall, creating a small recirculation zone (arrow A) immediately after the stenosis and a large recirculation zone (arrow B) further downstream of the stenosis. After the impingement, the outer part of the shear layer of the jet is totally annihilated, whereas the inner part of the shear layer eventually develops an instability and undergoes periodic vortex shedding (arrow C) in the ascending aorta. These vortex structures gradually break down into smaller vortices as they travel further downstream. Apart from the post-stenotic jet, the streamwise vorticity also demonstrates that there are strong secondary flows

developing in the ascending aorta due to its curvature [34]. Detailed analysis in Ref. [1] shows that both the instability of the post-stenotic jet as well as the secondary flow contribute to the wall pressure fluctuations.

Since the wall pressure fluctuations are responsible for the generation of the murmurs, monitor points are placed across the anterior surface of the aortic arch (marked by the solid red squares in Fig. 3a) during the hemodynamic simulations. The temporal history of the wall pressure is recorded at these points and used to determine the intensity of the wall pressure fluctuations as shown in Fig. 3b. The reason we focus on the anterior surface is that it directly faces the precordium (anterior surface) where the murmur signals are measured. Fig. 3 summarizes the source locations of the three cases studied here, which is defined as the location with highest pressure fluctuation intensity. It can be seen that they are clustered within 0.6*D* of each other, indicating a very weak dependence between the source location and the severity of the stenosis. This observation is important in clinical practice, since the source location, if determined accurately, may help to distinguish aortic stenosis from other heart conditions that generate systolic murmurs [23].

Another important aspect of the post-stenotic flow is the characteristic frequency generated by the flow. It is known that the shear layer instability of either confined or free round jets results in a discrete frequency vortex shedding at a Strouhal number (define as $St_j = fD_j/V_j$) around 0.60 [35, 36]. For the current study, since the jet is no longer circular after the impingement, a shedding Strouhal number (St_j) of 0.93 is observed when measured directly inside the jet (arrow C in Fig. 2) for all three cases

here. This shedding frequency also exists in spectra of the pressure signals collected at the source location in the form of a break frequency, as shown by the example in Fig. 4a. As a matter of fact, the break frequency of 0.93 is present in the pressure spectra at the source locations for all three cases (see Fig. 4b), indicating a strong contribution from the discrete frequency shear layer vortex shedding [1].

3.2 Murmur Propagation for 75% Stenosis Case

Fig. 5 demonstrates the wave pattern inside the tissue through contours of the instantaneous velocity. It clearly shows the generation of elastic waves at the interface of the aorta and the tissue, as well as the propagation of these waves inside the tissue. On the frontal plane, a distinct wave pattern is observed between 45^o and 90^o (the angle is measured from the end of the stenosis toward the ascending aorta as shown in Fig. 3a). However, in clinical practice, doctors can only measure signals on the epidermal surface with the help of a stethoscope or other similar sensors. In order to mimic this in the simulations, four surface monitor points are placed across the epidermal surface of the modeled thorax (see Fig. 5), and the signals at these locations are recorded during the simulation. Since a traction free boundary condition is applied at the surface, these monitor points essentially mimic minimal-load point sensors [5, 16]. The temporal histories of the wall-normal velocity perturbations are plotted in Fig. 6, and the wall-normal velocity is defined as $u_n = u_x n_x + u_y n_y + u_z n_z$, where (n_x, n_y, n_z) is the unit surface norm. The signal at location A has visibly stronger perturbations as it lies almost directly above the actual source location.

Spectra of the wall-normal acceleration calculated from these temporal signals are plotted in Fig. 7. Apart from the location D, the spectra from the other three locations share very similar trend. The amplitude first increases gradually as the frequency increases up to $St \approx 5 \times 10^{-3}$. The spectra then exhibit a short plateau before dropping sharply after $St \approx 2 \times 10^{-2}$. The acoustic break frequency can therefore be identified around $St = 2 \times 10^{-2}$ for this case. It should be emphasized that the break frequency defined here is associated with the murmur signal detected on the skin surface.

Based on the trend of the murmur spectra, the frequency range is separated into the three bands indicated in Fig. 7, and they are:

I: $f \in (10,20]Hz$; or $St \in (2.5 \times 10^{-3}, 5 \times 10^{-3}]$;

II: $f \in (20,80]Hz$; or $St \in (5 \times 10^{-3}, 2 \times 10^{-2}]$;

III: $f \in (80,400]Hz$; or $St \in (2 \times 10^{-2}, 10^{-1}]$.

The low frequency band starts from 10*Hz* assuming that the energy above the tenth harmonics of the cardiac cycle is not heavily influenced by whether the inflow is steady or pulsatile. One intuitive way to predict the source location of the murmurs is to inspect the intensity distribution of the surface signals. The underlying rationale is that for such a simple geometry and material model, the epidermal surface directly above the source location is expected to receive the strongest signal. The intensity of the signal in the frequency band $[f_1, f_2]$ can be quantified by the band-limited spectral energy, which is defined as $a_n^2 = \sum_{f_1}^{f_2} |\langle a_n \rangle(f)|^2$, where $\langle \quad \rangle$ represents the Fourier transform. As the monitor points are placed across the entire epidermal surface, we are able to

calculate the band-limited spectral energy over the entire anterior/posterior surface and project the three-dimensional surface onto a two-dimensional plane as shown in Fig. 8. The outline of the modeled aorta is also included here for clarity. The energy peak on these plots not only indicates the location on the epidermal surface with strongest acoustic signals but also serves as the prediction of source location on the modeled aorta.

Fig. 8a shows the energy distribution over the entire frequency band, and two peaks with similar magnitudes are observed. One is located above the ascending aorta region and overlaps with the correct source location, while the other one is above the outlet of the modeled aorta. It is clear from the hemodynamic study [1] and the wave pattern inside the thorax (see Fig. 5) that the outlet of the aorta is not a source location. Also, based on the previous study [10, 11], compression waves are convenient for predicting the source location due to its long wave length and better directionality. On the other hand, the shear wave can cause incorrect prediction due to the orthogonality between its propagation direction and the oscillation direction of the local material element. Similar conclusions can also be drawn from the current three-dimensional case. As shown in Fig. 8b, the surface energy contours show a single peak in the vicinity of the actual source location when shear wave propagation is excluded from the acoustic model. Therefore, the second peak in Fig. 8a is a consequence of the inclusion of the shear wave and the limited domain size. Given the expense of these simulations, we have not been able to explore the effect of a larger domain size on the simulations.

Moreover, in Fig. 9a, the spectra energy distribution in the low frequency band (I) is plotted, and the peak predicts the source location reasonably well. The energy at the false source location becomes stronger as the frequency increases (Fig. 9b,c). This deterioration of prediction accuracy is related to the alternating dominance of shear and compression waves at different frequency bands[11, 22]. At the low frequency band, the compression wave has strength comparable to the shear wave, and its long wavelength provides better directionality for source localization. On the other hand, the shear wave dominates the middle frequency band, leading to incorrect predictions, while the short wavelength of high frequency wave might make it more susceptible to the wall effect and ineffective in source localization.

3.3 Effects of the Severity of Stenosis

The focus of this study is on two particular aspects of auscultation: the first one is regarding the localization of the murmur source from surface signals, and the second is the connections between the source spectra and the murmur spectra. In this section, the results of the three different degrees of stenosis, 50%, 62.5% and 75% are presented in order to explore these two aspects.

Apart from the aortic stenosis, several other heart conditions are known to generate systolic murmurs, such as obstructive hypertrophic cardiomyopathy, mitral valve regurgitation, pulmonary valve stenosis and tricuspid insufficiency. However, the source of the murmur usually localizes in the vicinity of the underlying pathology, a fact that clinicians know and exploit in their assessment. For example, murmurs originating from the mitral valve are heard best near the cardiac apex; murmurs generated by the

pulmonary valve disease are usually best heard in the second and third left interspaces close to the sternum; and murmurs arising from the tricuspid valve are detected best around the lower left sternal border [37].

According to our previous study of the hemodynamics of the current configuration [1], the source locations for all three severities localize downstream of the stenosis and are within 0.6*D* of each other (see Fig. 3). This suggests that the source location of the aortic stenosis is relatively insensitive to its severity and, within the context of automated auscultation, this could potentially be used to determine whether a systolic murmur is caused by an aortic stenosis. It is already shown in Fig. 9a that the low-frequency-band spectral energy distribution on the epidermal surface has predicted a source location that is sufficiently close to the actual location for 75% case. Fig. 10a and Fig. 10b plot the same energy distribution for 50% and 62.5% case. These figures show that the energy peak directly above the modeled aorta predict a similar source location for different severities, and these locations lie in close proximity to the actual source locations. It is noted that there is also a local maximum located on the left lateral surface for the 50% stenosis case. This peak is generated due to the strong pressure fluctuations inside small recirculation area (arrow A in Fig. 2). However, this peak can be easily dismissed as a source location since it is not spatially correlated with the modeled aorta. Also, whether this peak is still visible in a physiologically accurate thorax models is questionable due to the presence of the lungs.

Another important aspect of auscultation is the spectral characteristics of the murmurs. As mentioned before, researchers have long believed that the break

frequency of the murmurs carries information about severity of the stenosis [4]. In the current study, there is no clear preferred location to study the frequency since the break frequency can be observed over a wide spatial range (see Fig. 7). In order to make the study consistent, signals measured at the location of the black diamond symbols in Fig. 9a, Fig. 10a and Fig. 10b are used to calculate the spectra shown in Fig. 11. These three spectra share similar trends: the amplitude first increases as the frequency increases; this is followed by a plateau and then subsequently a sharp decrease with increasing frequency. The acoustic break frequency is generally around $St = 2 \times 10^{-2}$ for the three cases but decreases slightly as the severity decreases.

It is useful to understand the difference between the signal spectra from the flow and the acoustic studies. In Fig. 12, the murmur spectra from Fig. 11 are renormalized by the jet velocity and jet diameter. Compared with Fig. 4b, it can be seen that the propagation inside the tissue alters the source spectra significantly. The low frequency band energy is much lower in the murmur signal while the sharp slope change around the break frequency is more clearly defined in the murmur spectra than the source spectra. Moreover, there is no clear connection between the hemodynamic break frequency and the acoustic break frequency. This is especially true for the 50% and 62.5% case, as $St_j = 0.93$ lies in the plateau of the murmur spectra. These discrepancies between the flow and acoustic spectra clearly reveal the importance of understanding the propagation of the murmurs.

3.4 Discussion

The previous section presents the results from the hemoacoustic simulations. In this section, motivated by the studies in Refs. [22, 38], we try to gain a better understanding of the results from a more theoretical perspective with the help of the free-space Green's function. Compared to the vector decomposition proposed in Ref. [11], the free-space Green's function can provide insights into the shear wave and compression wave behavior at a significantly lower computational cost. The free-space Green's function for the current homogeneous, linear viscoelastic material is summarized in the Appendix. With the help of this function, the murmur spectrum at the skin surface is approximated using the pressure fluctuations on the aortic lumen wall (i.e. the 'forward' problem) in Section 3.4.1. In Section 3.4.2 we explore the possibility of localizing the murmur source from the acoustic signals collected at the skin surface using the free-space Green's function (i.e. the 'inverse' problem).

3.4.1 Forward Problem

In the forward problem, the pressure recorded on the wall of the modeled aorta is used to evaluate the signal at the epidermal surface of the thorax. Instead of finding the Green's function for the current problem, i.e. a point source inside an elliptical cylinder, the free-space Green's function is used to approximate the solution. The same practice is adopted in Refs. [22, 38]. It is noted that even though using the free-space Green's function doesn't take into consideration of the shear/compression wave conversion at the surface, it has been found to provide a reasonable agreement with the numerical and experimental studies of a similar problem [22].

The set-up of the problem is illustrated in Fig. 13. The surface force in Eq. (A4) is replaced with a distribution of 37 point sources on the lumen surface (black squares in Fig. 13) which are spaced 5° away from each other on both the anterior surface and the posterior surface of the aorta. The temporal histories of the pressure on these points are recorded and serve as the point sources in calculating the resulting acoustic signal at a given point in space through the following equation

$$\frac{\langle a_n \rangle(\vec{x},\omega)}{\Delta \mathrm{A}} = 2\sum_{j=1}^{J}(i\omega)^2 N_p G_{pq}\left(\vec{x}-\vec{X}_j,\omega\right)M_q\left(\vec{X}_j\right)\langle P\rangle\left(\vec{X}_j,\omega\right). \qquad (2)$$

Here, J is the total number of point sources, and it equals 74 (from both anterior and posterior surface) in this study. $\vec{X}_j$ is the coordinate of the *j*-th point source, and $\vec{x}$ is the coordinate of the target point on the epidermal surface of the thorax, which is chosen to correspond to the location of the black diamond symbol in Fig. 9a. $\vec{M}(\vec{X})$ and $\vec{N}(\vec{x})$ are the unit normal vector at the locations of the point source and the target point, respectively. Finally, $P(\vec{X})$ is the hydrodynamic pressure force at point source $\vec{X}$. The indices p and q range from 1 to 3 and ΔA is the surface area occupied by each point source. The multiplicative factor of two preceding the summation is a crude approximation of the wave reflection at the epidermal surface based on the suggestion in Ref. [38].

Fig. 14a shows the results for all three cases, and the spectra demonstrate significant similarity to the results from the hemoacoustic simulations in Fig. 11. Moreover, the acoustic break frequencies based on the approximations match those from the numerical simulations reasonably well, and they show the same slight

decrease with decrease in severity. The above observation clearly shows that 74 point sources are sufficient to capture the characteristics of the spectra of the wall-normal acceleration. This also indicates that, at least in this case, the geometry of the modeled thorax is not the determining factor for the shape of the spectra and the break frequency in particular. Fig. 14 is the result of all the point sources superimposed at the target location, while Fig. 15 shows the contribution from individual point source at selected angle θ for 75% case. It is apparent that the spectra generated from single point source does not exhibit the aforementioned shape and break frequency, which echoes the finding of Fredberg [14] that it is the superimposition of murmurs generated at different locations of the modeled aorta that determines the shape of the final spectrum. Thus, using a single point source, even the one at the dominant source location, does not provide a reasonable representation of the overall signal in experimental or numerical studies.

3.4.2 Inverse Problem

Since the free-space Green's function performs relatively well in terms of predicting the shape of the spectra of the murmur signals, it should be possible to use it to synthesize a source localization methods. Fig. 16 illustrates the process of the source localization, i.e. using the surface signal collected from the acoustic simulations to locate the source of the murmurs. During the acoustic simulations, wall-normal accelerations are recorded on the epidermal surface at different locations. Assuming there are K monitor points in total, we have

$$\langle a_n\rangle(\vec{x}_k,\omega)=\sum_{j=1}^{J}\underbrace{(i\omega)^2N_p(\vec{x}_k)G_{pq}\big(\vec{x}_k-\vec{X}_j,\omega\big)M_q\big(\vec{X}_j\big)\Delta\mathrm{A}}_{\mathcal{G}(\vec{x}_k-\vec{X}_j,\omega)}\langle P\rangle\big(\vec{X}_j,\omega\big), \tag{3}$$

All the parameters have the same meanings as before, except that now $\langle a_n\rangle$ is known, and $\langle P\rangle$ is unknown. The distribution of the pressure will reveal the source location. Employing the following short-hand f_k, f_j and f_{kj} for $f(\vec{x}_k)$, $f(\vec{X}_j)$ and $f(\vec{x}_k-\vec{K}_j)$ respectively. We have

$$\langle a_n\rangle_k(\omega)=\mathcal{G}_{kj}(\omega)\langle P\rangle_j(\omega). \tag{4}$$

$\mathcal{G}$ is a matrix of size $K\times J$, where K is the number of monitor points while J is the number of point sources. Generally, these two number are not necessarily equal, and hence the pressure distribution at angular frequency ω can be expressed as

$$\langle P\rangle_j(\omega)=\big[\mathcal{G}_{kj}(\omega)\big]^{\perp}\langle a_n\rangle_k(\omega). \tag{5}$$

where $\perp$ represents Moore-Penrose pseudo-inverse [39].

During the hemoacoustic simulations of 75% case, 16 evenly spaced monitor points (mimicking an array of sensors[8,24]) are placed on the epidermal surface of the modeled thorax with the spacing in y direction being $1.5D$ and the spacing in z direction being $1.3D$. The potential source location resides in the frontal plane (marked as green in Fig. 16) and the plane is evenly discretized by 25 mesh points with spacing $0.625D$ in each direction. It is noted that Eq. (5) is frequency dependent, and thus, for each angular frequency ω, a system of equations that can be solved to obtain the amplitude of the pressure. We have already observed from the study in Section 3.3 that the signal intensity of frequency band I is spatially well correlated with the murmur source.

Therefore, the wall-normal acceleration at the lower frequency band is used to calculate the band-limited energy distribution of the pressure by

$$P^2 = \sum_{\frac{\omega}{2\pi}\in \mathrm{I}} \left\{ \left[\mathcal{G}_{kj}(\omega) \right]^{\perp} \langle a_n \rangle_k (\omega) \right\}^2 . \tag{6}$$

The result is plotted in Fig. 17. It can be seen that this prediction does a reasonable job of placing the expected source location downstream of the modeled aorta and in the vicinity of the actual source location.

4. CONCLUSIONS

In this study, a high-order immersed boundary method based acoustic solver is used to simulate the propagation of murmurs generated by a modeled aorta with an aortic stenosis. The wall pressure on the modeled aorta is applied as the boundary condition in the acoustic simulations. Three cases with stenoses ranging from mild to borderline severe (50%, 62.5% and 75%) are investigated in order to gain better understanding of the murmur propagation. The source locations predicted by the acoustic signal intensity on the skin surface and the free-space Green's function are in good agreement with the actual locations determined in the hemodynamic studies. The fact that this source location is relatively insensitive to the severity of the stenosis makes it a potential diagnostic criterion to differentiate aortic stenosis from other heart conditions that generate systolic murmurs. The spectral analysis of the wall normal acceleration at the skin surface shows a break frequency for all three cases study here. This break frequency is a consequence of the superimposition of murmurs generated from wall pressure fluctuations at different locations on the modeled aorta. It is important to note

that this break frequency generally does not equal to the underlying jet shear layer shedding frequency, i.e. the hemodynamic break frequency.

Finally, we note that the current study has several limitations. First, by assuming a steady inflow into the aorta we might be missing effects associated with the pulsatile nature of the aortic jet. This effect of the pulsatility on the generation and propagation of the murmurs is currently being explored. Second, the current model is highly simplified in terms of geometry and material properties. The geometric simplifications of the aorta model and their potential effects are discussed in Ref [1]. The major simplification of the thorax model is neglecting the different organs/tissues, such as lungs and bones, and the associated material heterogeneity. The geometric and anatomical complexities of the thorax can in-principle be included in the current method [22]. Due to the large size and low density, lungs are expected to be the major obstacle for murmur propagation. Furthermore, the thoracic organs and tissues may also introduce complex frequency components into the spectrum as shown in Ref. [22]. Murmur propagation through a realistic thorax model is being investigated and will be reported in the future.

ACKNOWLEDGMENT

The authors acknowledge the financial support from NSF Grants IIS-1344772 and CBET 1511200, and computational resource by XSEDE NSF Grant TG-CTS100002, the Maryland Advanced Research Computing Center (MARCC).

FUNDING

This study is supported by National Science Foundation (NSF) grants IIS-1344772 and CBET 1511200

APPENDIX

The governing equation for the elastic wave generation by a point source at the origin can be expressed as follows:

$$\rho_s \frac{\partial^2 v_i}{\partial t^2} - \frac{\partial}{\partial x_j}\left[\lambda \frac{\partial v_k}{\partial x_k}\delta_{ij} + \mu\left(\frac{\partial v_i}{\partial x_j} + \frac{\partial v_j}{\partial x_i}\right)\right] = s_i(t)\delta(\vec{x}), \tag{A1}$$

where v_i is the displacement vector, $s_i(t)$ is the source vector, and $\delta(\vec{x})$ is the Dirac delta function used to localize the source. If the wave is propagating freely in the space, its behavior can be described in the frequency domain with the help of the free-space Green's function $G_{ij}(\vec{x}, \omega)$

$$\langle v_i\rangle(\vec{x}, \omega) = G_{ij}(\vec{x}, \omega)\langle s_j\rangle(\omega), \tag{A2}$$

where $\langle\ \ \rangle$ represents the Fourier transform of the function, and ω is the angular frequency. The Green's function in the three-dimensional space corresponding to Eq. (A1) has the following expression [40]

$$G_{ij}(\vec{x}, \omega) = \frac{ik_p}{12\pi(\lambda + 2\mu)}\left[h_0^{(1)}(k_p r)\delta_{ij} + \left(\delta_{ij} - \frac{3x_i x_j}{r^2}\right)h_2^{(1)}(k_p r)\right] \tag{A3}$$

$$- \frac{ik_s}{12\pi\mu}\left[-2h_0^{(1)}(k_s r)\delta_{ij} + \left(\delta_{ij} - \frac{3x_i x_j}{r^2}\right)h_2^{(1)}(k_s r)\right],$$

where $h_n^{(1)}$ is the spherical Hankel function of the first kind, and k_p, k_s, r are defined as

$$k_p = \omega/c_p, \qquad k_s = \omega/c_s, \qquad r = |\vec{x}|.$$

k_p and k_s can be interpreted as the compression and shear wave number, respectively. It is easily observed that the first term of the Green's function describes the propagation of the generated compression wave, while the second term is solely responsible for the propagation of the shear wave. In the above equation, the source is located at the origin, while in this study, the source is the pressure force distributed on the lumen wall of the aorta.

The acceleration can be expressed as $\langle a_i \rangle(\vec{x}, \omega) = (i\omega)^2 G_{ij}(\vec{x}, \omega)\langle s_j \rangle(\omega)$. Thus, for a general two-dimensional surface A in a three-dimensional space, the acceleration at any location can be written as

$$\langle a_p \rangle(\vec{x}, \omega) = \int_A (i\omega)^2 G_{pq}\big(\vec{x} - \vec{X}, \omega\big)\langle P \rangle\big(\vec{X}, \omega\big) M_q\big(\vec{X}\big)\mathrm{d}A, \qquad \text{(A4)}$$

where *p, q* are indices ranging from 1 to 3, $\vec{x}$ is a random point in the space and $\vec{X}$ is a point on the lumen surface A. $P(\vec{X})$ is the hydrodynamic pressure force at $\vec{X}$ and $\vec{M}(\vec{X})$ is the unit normal vector at the same location. The effect of viscosity can be included by replacing the second Lame constant μ with $\mu_{effective} = \mu - i\omega\eta$.

REFERENCES

[1] C. Zhu, J.H. Seo, and R. Mittal, "Computational modelling and analysis of haemodynamics in a simple model of aortic stenosis," *J. Fluid Mech.*, vol. 851, pp. 23–49, 2018.

[2] I. R. Hanna and M. E. Silverman, "A history of cardiac auscultation and some of its contributors," *Am. J. Cardiol.*, vol. 90, no. 3, pp. 259–267, 2002.

[3] R. S. Lees and C. F. Dewey, "Phonoangiography: a new noninvasive diagnostic method for studying arterial disease.," *Proc. Natl. Acad. Sci. U. S. A.*, vol. 67, no. 2, pp. 935–942, 1970.

[4] G. W. Duncan, J. O. Gruber, C. F. Dewey Jr, G. S. Myers, and R. S. Lees, "Evaluation of carotid stenosis by phonoangiography," *N. Engl. J. Med.*, vol. 293, no. 22, pp. 1124–1128, 1975.

[5] J. Semmlow and K. Rahalkar, "Acoustic detection of coronary artery disease," *Annu. Rev. Biomed. Eng.*, vol. 9, pp. 449–69, Jan. 2007.

[6] P. Erne, "Beyond auscultation--acoustic cardiography in the diagnosis and assessment of cardiac disease.," *Swiss Med. Wkly.*, vol. 138, no. 31–32, pp. 439–52, 2008.

[7] R. L. Watrous, W. R. Thompson, and S. J. Ackerman, "The impact of computer-assisted auscultation on physician referrals of asymptomatic patients with heart murmurs," *Clin. Cardiol.*, vol. 31, no. 2, pp. 79–83, 2008.

[8] A. G. Andreou, T. Abraham, W. R. Thompson, J. H. Seo, and R. Mittal, "Mapping the cardiac acousteome: An overview of technologies, tools and methods," in *49th Annual Conference on Information Sciences and Systems (CISS),* 2015.

[9] H. Bakhshaee, G. Garreau, G. Tognetti, K. Shoele, R. Carrero, T. Kilmar, C. Zhu, W. R. Thompson, J. H. Seo, R. Mittal, and A. G. Andreou, "Mechanical design, instrumentation and measurements from a hemoacoustic cardiac phantom," in *49th Annual Conference on Information Sciences and Systems (CISS),* 2015.

[10] J. H. Seo and R. Mittal, "A coupled flow-acoustic computational study of bruits from a modeled stenosed artery.," *Med. Biol. Eng. Comput.*, vol. 50, no. 10, pp. 1025–35, Oct. 2012.

[11] C. Zhu, J.H. Seo, H. Bakhshaee, and R. Mittal, "A Computational Method for Analyzing the Biomechanics of Arterial Bruits," *J. Biomech. Eng.*, vol. 139, no. 5, p. 051008, 2017.

[12] R. Tobin and I. Chang, "Wall pressure spectra scaling downstream of stenoses in steady tube flow," *J. Biomech.*, vol. 9, no. January, pp. 633–640, 1976.

[13] R. Mittal, S. P. Simmons, and F. Najjar, "Numerical study of pulsatile flow in a constricted channel," *J. Fluid Mech.*, vol. 485, pp. 337–378, 2003.

[14] J. J. Fredberg, "Pseudo-sound generation at atherosclerotic constrictions in arteries," *Bull. Math. Biol.*, vol. 36, no. 2, pp. 143–155, 1974.

[15] N. L. Owsley and A J. Hull, "Beamformed nearfield imaging of a simulated coronary artery containing a stenosis.," *IEEE Trans. Med. Imaging*, vol. 17, no. 6, pp. 900–9, Dec. 1998.

[16] D. B. Cooper, M. J. Roan, and P. P. Vlachos, "Acoustic source separation for the

detection of coronary artery sounds.," *J. Acoust. Soc. Am.*, vol. 130, no. 6, pp. 4158–66, 2011.

[17] S. A. Jones and A. Fronek, "Analysis of break frequencies downstream of a constriction in a cylindrical tube," *J. Biomech.*, vol. 20, no. 3, pp. 319–327, 1987.

[18] S. Ramakrishnan, S. Udpa, and L. Udpa, "A numerical model simulating sound propagation in human thorax," *2009 IEEE Int. Symp. Biomed. Imaging From Nano to Macro*, pp. 530–533, Jun. 2009.

[19] T. J. Royston, X. Zhang, H. a. Mansy, and R. H. Sandler, "Modeling sound transmission through the pulmonary system and chest with application to diagnosis of a collapsed lung," *J. Acoust. Soc. Am.*, vol. 111, no. 4, p. 1931, 2002.

[20] A. M. McKee and R. A. Goubran, "Sound Localization in the Human Thorax," in *Instrumentation and Measurement Technology Conference, 2005. IMTC 2005. Proceedings of the IEEE*, 2005.

[21] Y. Yazicioglu, T. J. Royston, T. Spohnholtz, B. Martin, F. Loth, and H. S. Bassiouny, "Acoustic radiation from a fluid-filled, subsurface vascular tube with internal turbulent flow due to a constriction," *J. Acoust. Soc. Am.*, vol. 118, no. 2, p. 1193, Aug. 2005.

[22] J. H. Seo, H. Bakhshaee, G. Garreau, C. Zhu, A. Andreou, W. R. Thompson, and R. Mittal, "A method for the computational modeling of the physics of heart murmurs," *J. Comput. Phys.*, vol. 336, 2017.

[23] A. Leatham, "Systolic Murmurs," *Circulation*, vol. 17, no. 4, p. 601 LP-611, Apr. 1958.

[24] C. Sapsanis, G. Tognetti, R. Mittal, G. Garreau, P.O. Pouliquen, W.R. Thompson, A. G. Andreou, "StethoVest: A simultaneous multichannel wearable system for cardiac acoustic mapping," in *Proceedings 2018 IEEE Biomedical Circuits and Systems Conference*, 2018, pp. 191–194.

[25] E. L. Yellin, "Hydraulic noise in submerged and bounded liquid jets," in *Biomedical Fluid Mechanics Symposium*, 1966, pp. 209–221.

[26] C. Clark, "Turbulent velocity measurements in a model of aortic stenosis," *J Biomech*, vol. 9, no. 11, pp. 677–687, 1976.

[27] R. Mittal, H. Dong, M. Bozkurttas, F. M. Najjar, A. Vargas, and A. von Loebbecke, "A versatile sharp interface immersed boundary method for incompressible flows with complex boundaries," *J. Comput. Phys.*, vol. 227, no. 10, pp. 4825–4852, Jan. 2008.

[28] J. H. Seo and R. Mittal, "A Sharp-Interface Immersed Boundary Method with Improved Mass Conservation and Reduced Spurious Pressure Oscillations.," *J. Comput. Phys.*, vol. 230, no. 19, pp. 7347–7363, Aug. 2011.

[29] C. Zhu, J. H. Seo, V. Vedula, and R. Mittal, "A highly scalable sharp-interface immersed boundary method for large-scale parallel computers," in *23rd AIAA Computational Fluid Dynamics Conference*, 2017.

[30] S. A. Ahmed and D. P. Giddens, "Velocity measurements in steady flow through axisymmetric stenoses at moderate Reynolds numbers," *J. Biomech.*, vol. 16, no. 7, pp. 505–516, Jan. 1983.

[31] S. A. Ahmed and D. P. Giddens, "Flow disturbance measurements through a

constricted tube at moderate Reynolds numbers," *J. Biomech.*, vol. 16, no. 12, pp. 955–963, 1983.
[32] R. A. Cassanova and D. P. Giddens, "Disorder distal to modeled stenoses in steady and pulsatile flow," *J. Biomech.*, vol. 11, no. 10–12, pp. 441–453, 1978.
[33] N. Edgar and M. Visbal, "A general buffer zone-type non-reflecting boundary condition for computational aeroacoustics," *AIAA-paper*, no. May, pp. 1–9, 2003.
[34] W. R. Dean, "Note on the motion of fluid in a curved pipe," *London, Edinburgh, Dublin Philos. Mag. J. Sci.*, vol. 4, no. 20, pp. 208–223, 1927.
[35] F. C. C. Johansen, "Flow through Pipe Orifices at low Reynolds Numbers," *Proc. R. Soc. London. Ser. A, Contain. Pap. a Math. Phys. character*, vol. 126, no. 801, pp. 231–245, 1929.
[36] G. S. Beavers and T. A. Wilson, "Vortex growth in jets," *J. Fluid Mech.*, vol. 44, pp. 97–112, 1970.
[37] L. Bickley and P. G. Szilagyi, *Bates' guide to physical examination and history-taking*. Lippincott Williams & Wilkins, 2012.
[38] T. J. Royston, Y. Yazicioglu, and F. Loth, "Surface response of a viscoelastic medium to subsurface acoustic sources with application to medical diagnosis.," *J. Acoust. Soc. Am.*, vol. 113, no. 2, pp. 1109–1121, 2003.
[39] A. Ben-Israel and T. N. E. Greville, "Generalized Inverses: Theory and Applications," *Int. Stat. Rev. / Rev. Int. Stat.*, 2002.
[40] A. Ben-Menahem and S. J. Singh, *Seismic waves and sources*. Springer Science & Business Media, 2012.

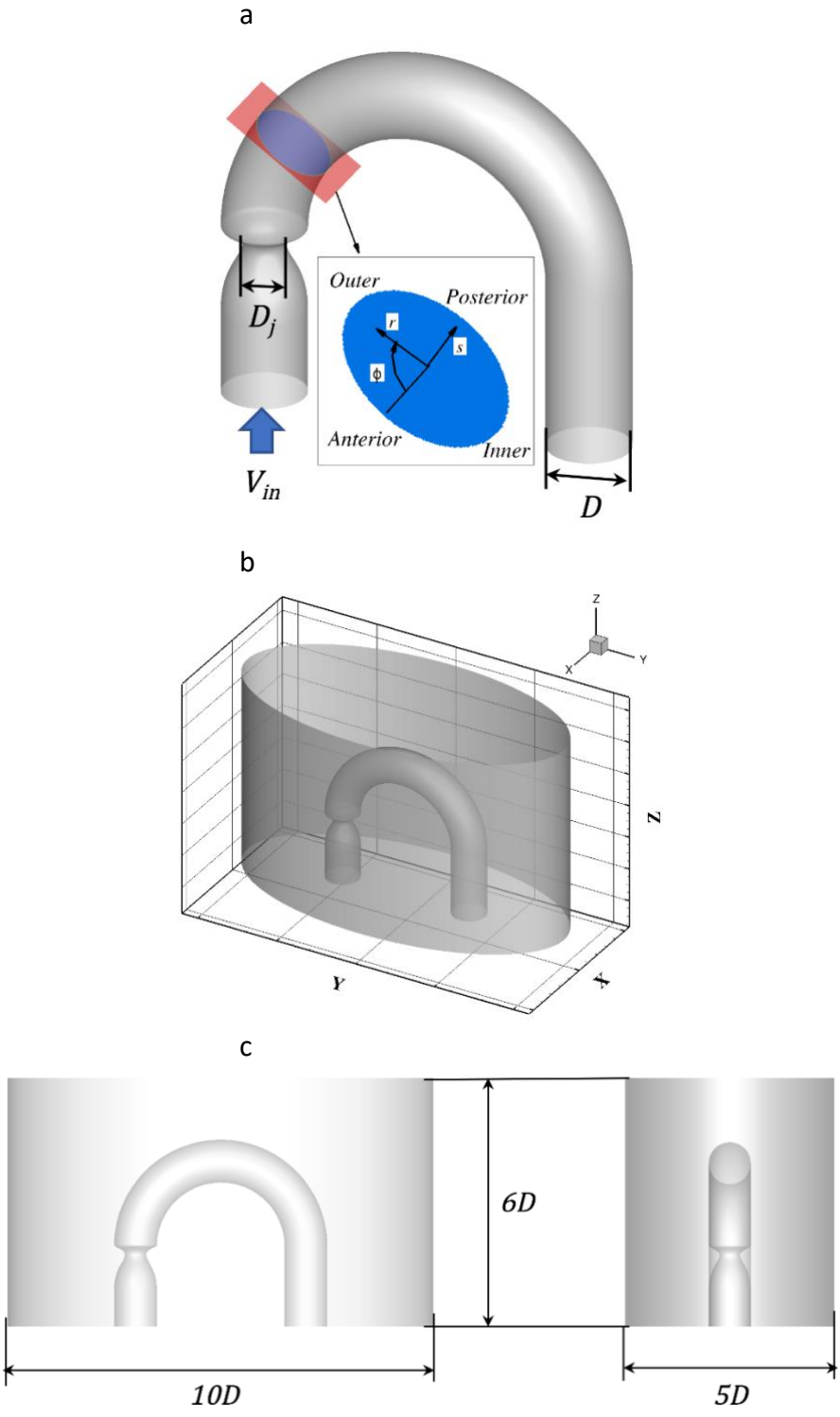

Fig. 1 (a) Schematic of the modeled aorta and *r, ϕ* and *s* represent the radial, azimuthal and streamwise direction; (b) schematic of the modeled thorax; (c) dimensions of the modeled thorax.

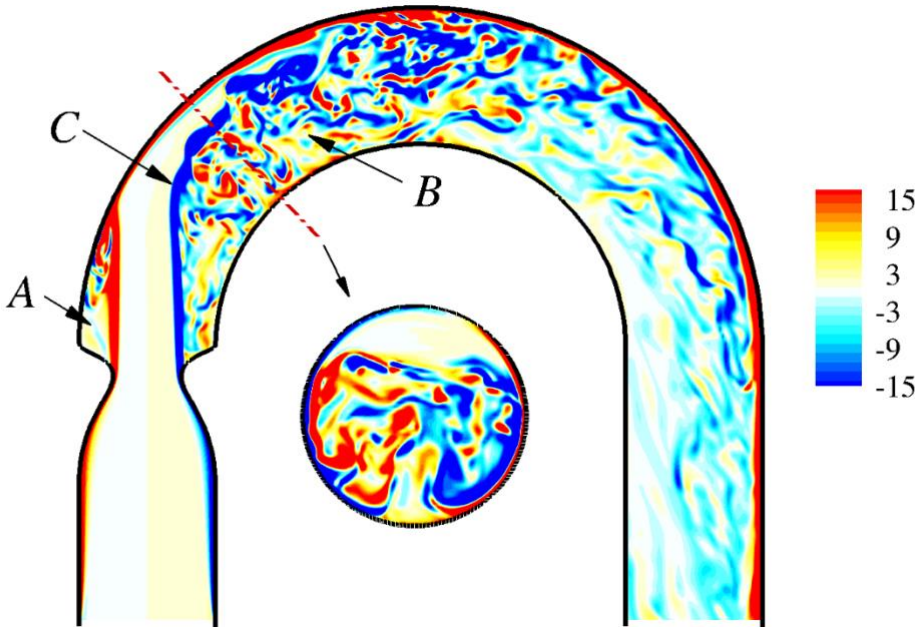

Fig. 2 Instantaneous azimuthal vorticity ($\omega_\phi D/V_{in}$) on the frontal plane as well as instantaneous streamwise vorticity ($\omega_s D/V_{in}$) on the cross-section of the modeled aorta with 75% stenosis. Arrow A: small recirculation zone; arrow B: large recirculation zone; arrow C: starting position of the periodic shear layer vortex shedding. This figure is adapted from Ref. [1].

a

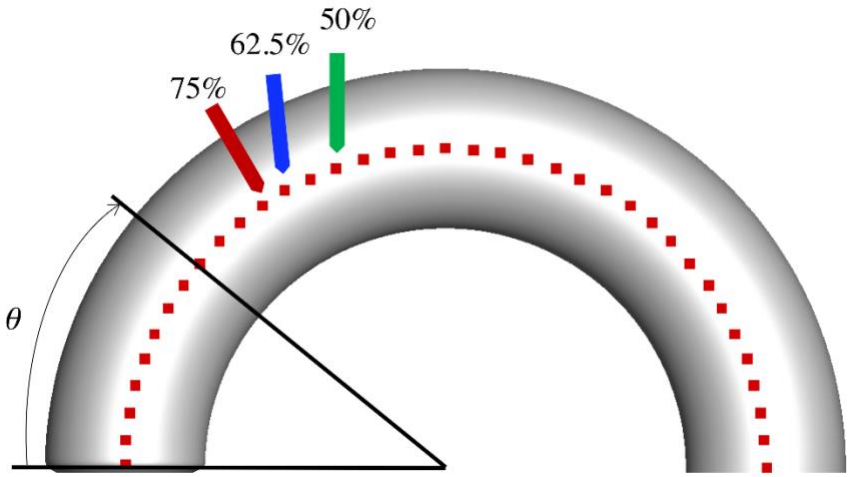

b

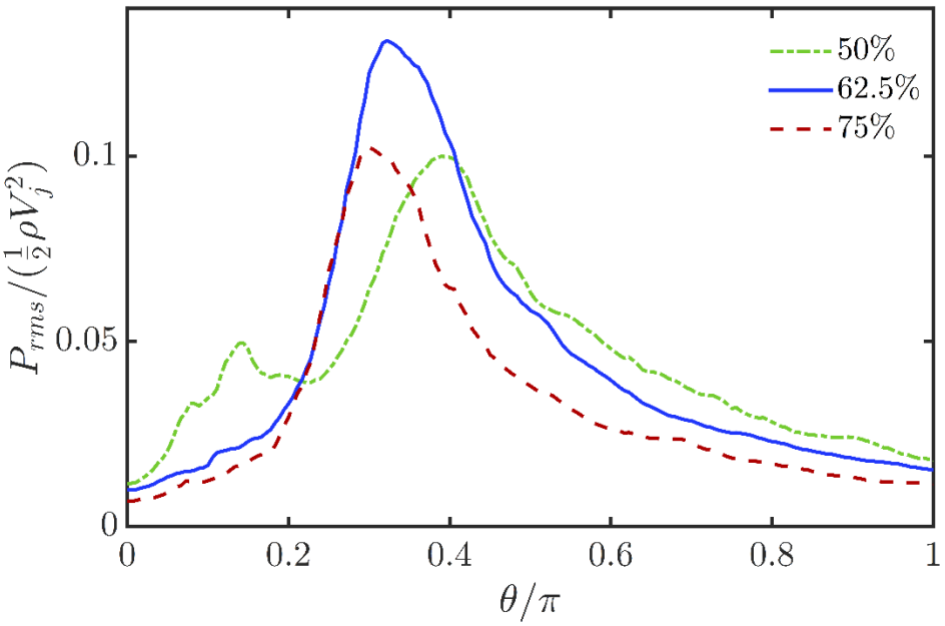

Fig. 3 (a) Summary of the source locations on the anterior surface of all three cases. The arrows at $\theta = 70°, 60°$ and $55°$ point to the source locations for *AS*=50%, 62.5% and 75%, respectively. (b) Distribution of pressure fluctuation intensity along the anterior surface, where the peak locations are identified as murmur sources and are highlighted in (a) with arrows. This figure is adapted from Ref. [1].

(a)

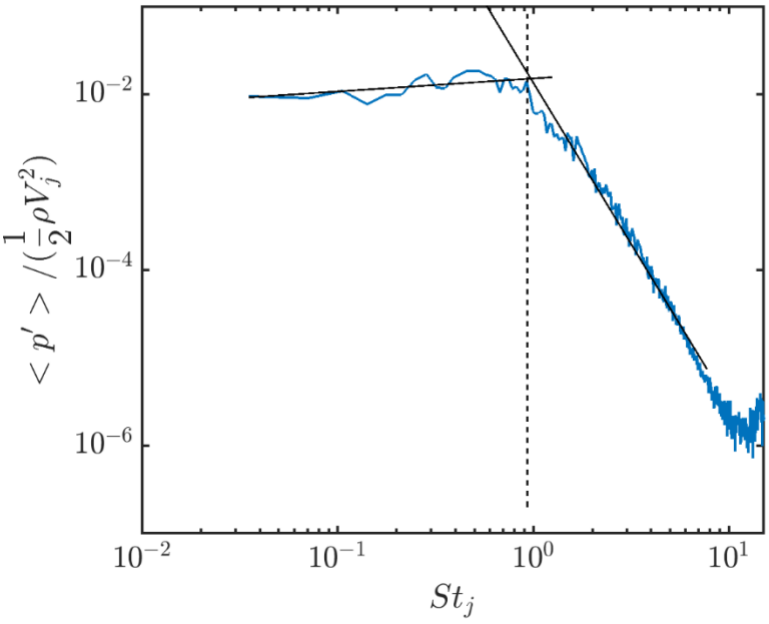

(b)

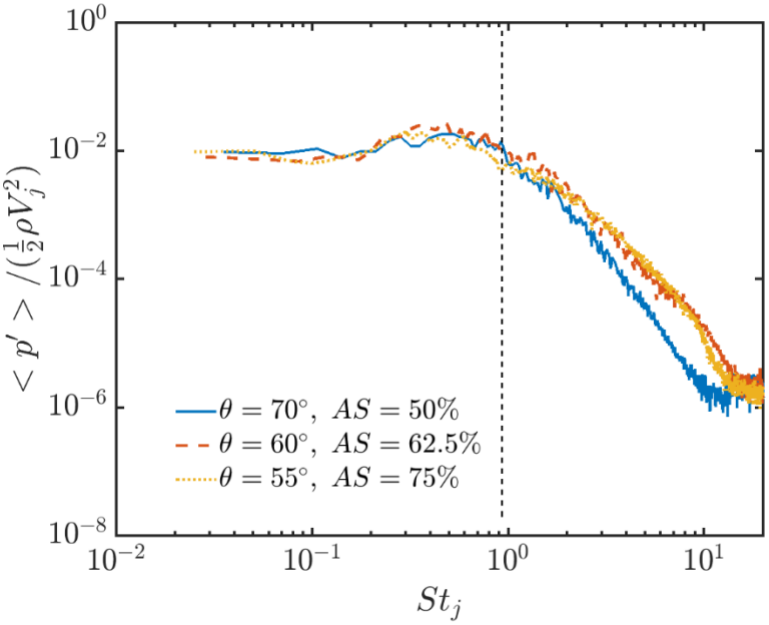

Fig. 4 (a) Spectrum of the pressure fluctuation at the source location of 50% case. (b) Spectra of wall pressure fluctuations for *AS*=50%, 62.5% and 75% at the source locations indicated in Fig. 3. Here the frequency is renormalized by the jet velocity (V_j) and jet diameter (D_j). The vertical dash line at $St_j = 0.93$ indicates the break frequency from flow simulation. The solid lines in (a) show the slope of the spectrum calculated by the linear regression. These figures are adapted from Ref. [1].

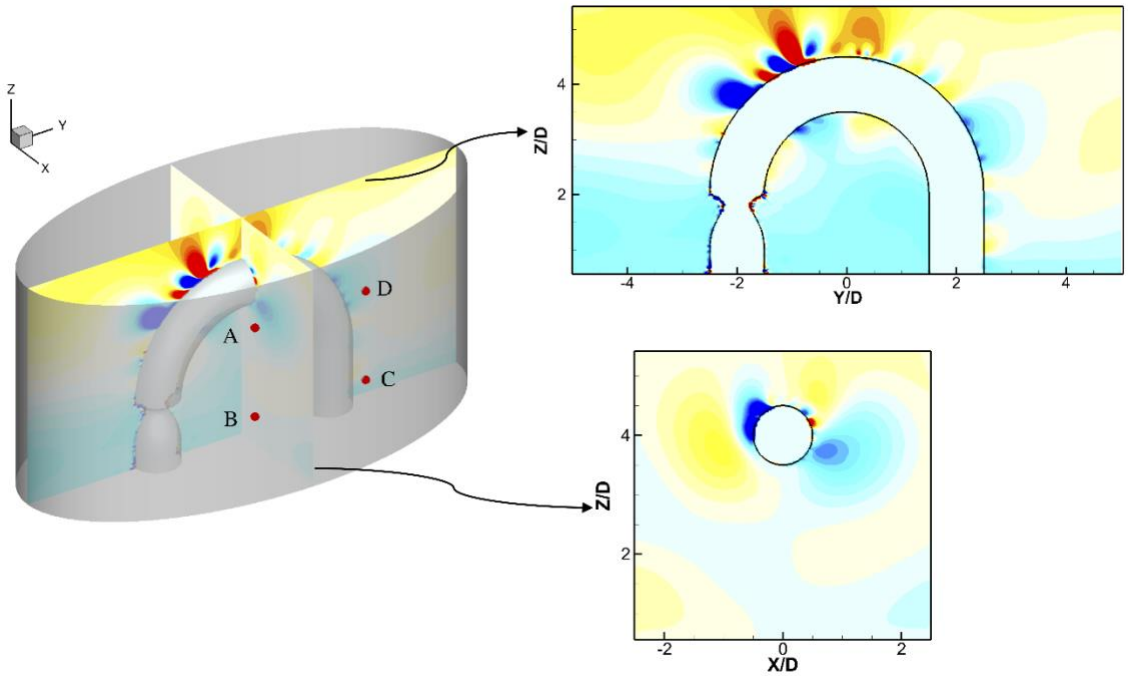

Fig. 5 Instantaneous wave pattern inside the modeled thorax with 75% stenosis demonstrated by the velocity contour. Frontal plane plots the velocity along the major axis (*y* direction) and the sagittal plane plots the velocity along the minor axis (*x* direction).

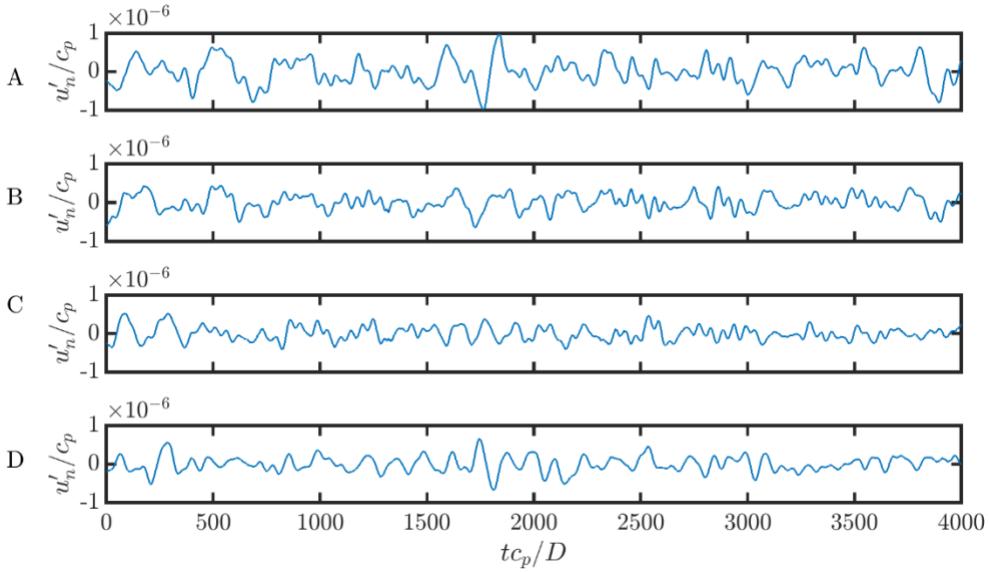

Fig. 6 Temporal histories of the wall-normal velocity perturbation recorded at the four surface locations shown in Fig. 5 for 75% stenosis. The same range of the y-axis $[-1 \times 10^6, 1 \times 10^6]$is used to facilitate comparison of signal intensity at these four locations.

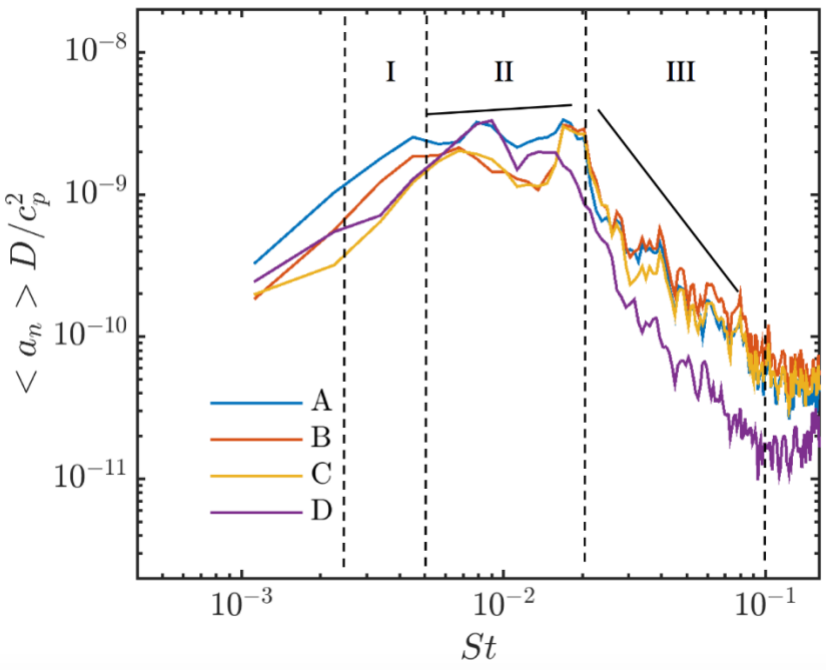

Fig. 7 Spectra of the wall-normal acceleration at the four surface locations shown in Fig. 5 for 75% stenosis. The Strouhal number is defined as $St = fD/c_p$.

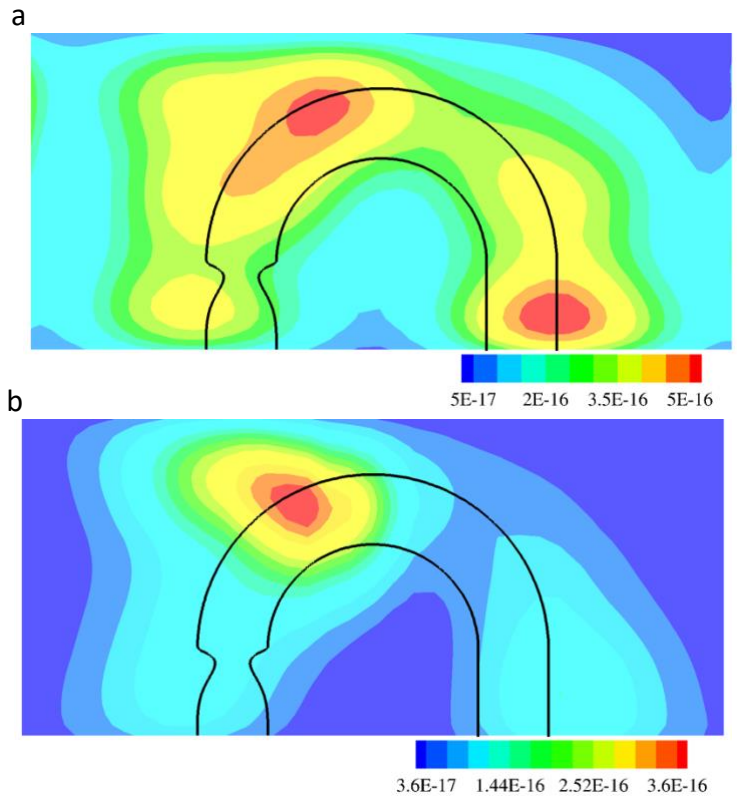

Fig. 8 Two-dimensional projection of the spectral energy of wall-normal acceleration on the anterior/posterior surface over the entire frequency band $(\mathrm{I} + \mathrm{II} + \mathrm{III})$ for 75% case. The range of the contours is adjusted to best reflect the signal intensity in each case and the outline of the modeled aorta is included for clarity. (a) With shear modulus; (b) without shear modulus.

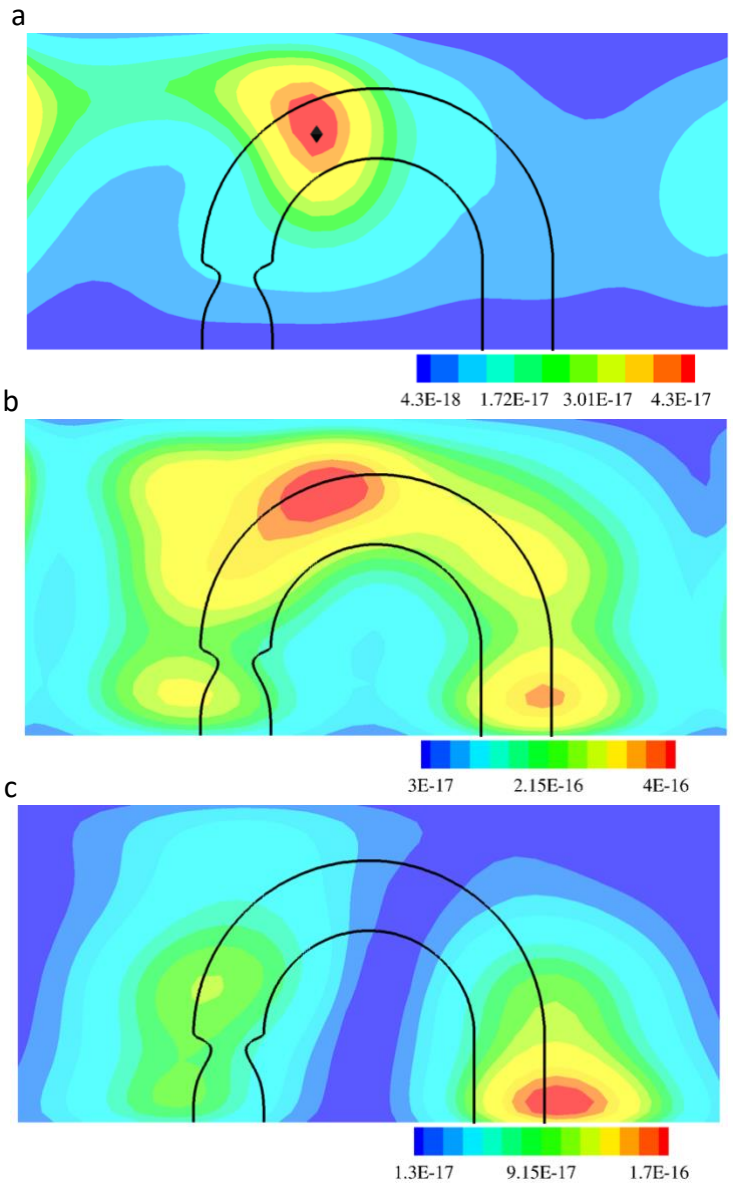

Fig. 9 Two-dimensional projection of the spectral energy of wall-normal acceleration on the anterior/posterior surface over different frequency bands for 75% case with shear modulus included in the model. The range of the contours is adjusted to best reflect the signal intensity for each frequency range and the outline of the modeled aorta is included for clarity. (a) frequency band I; (b) frequency band II; (c) frequency band III.

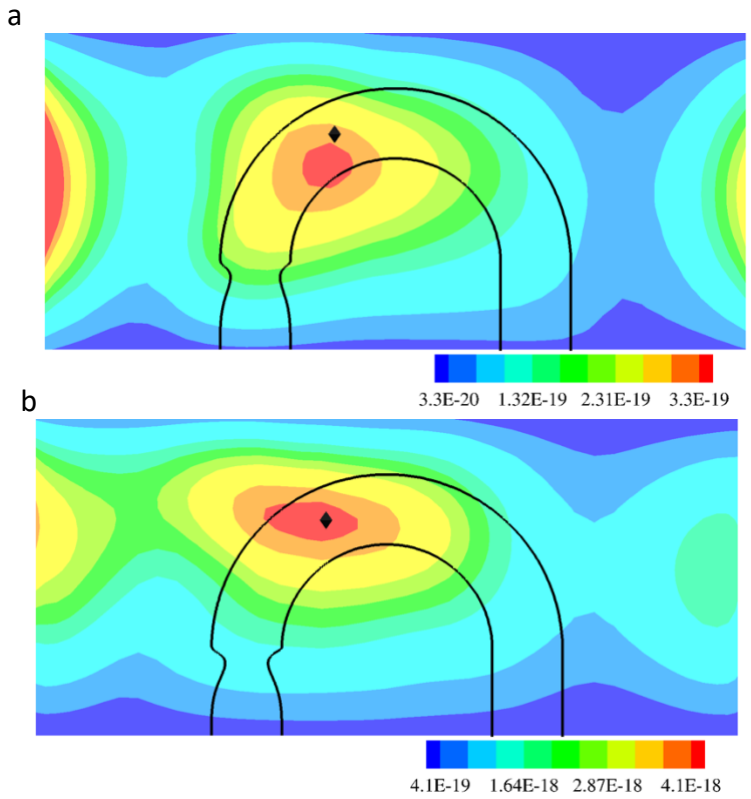

Fig. 10 Two-dimensional projection of the spectral energy of wall-normal acceleration on the anterior/posterior surface over the low frequency band I. A black diamond symbol is plotted in the same spatial location in Fig. 9a and Fig. 10 to facilitate comparison. (a) 50%; (b) 62.5%. Shear modulus is included in both models.

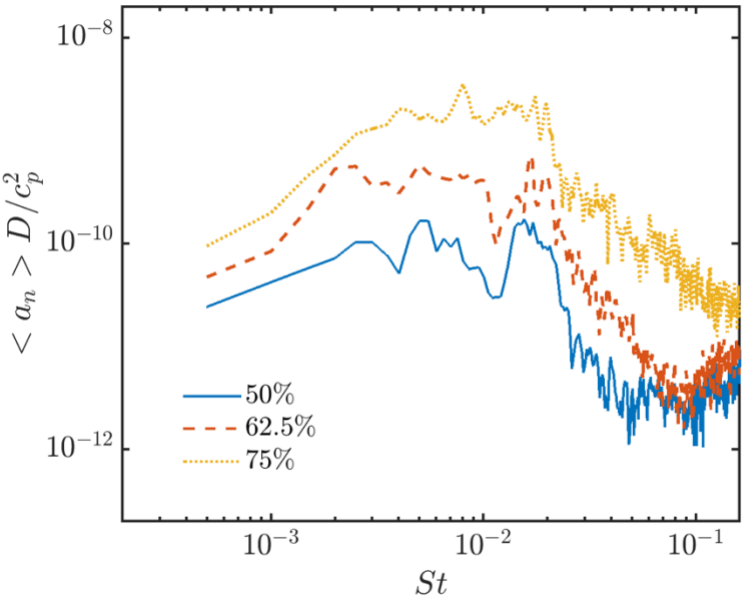

Fig. 11 Spectra of the wall-normal acceleration on the epidermal surface of the modeled aorta. The signals are collected at the same spatial location indicated by the black diamond symbol. The Strouhal number is defined as $St = fD/c_p$.

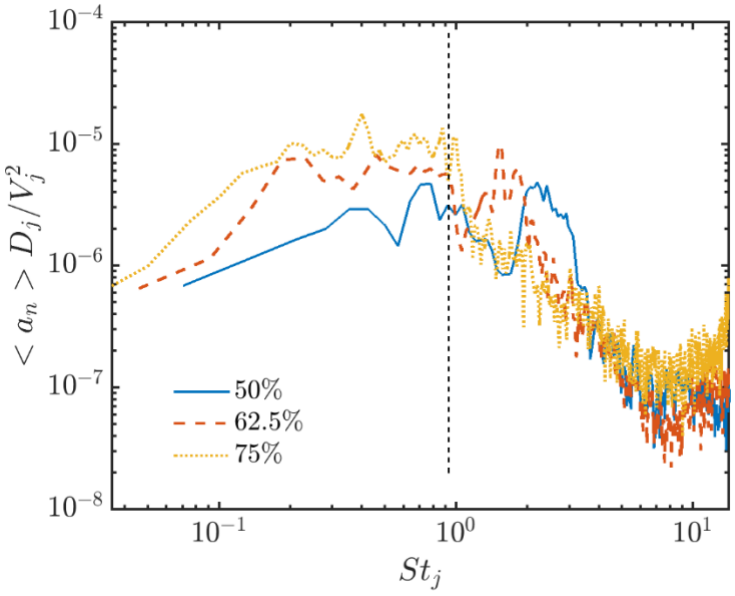

Fig. 12 Spectra of the wall-normal acceleration on the epidermal surface of the modeled aorta renormalized using jet velocity (V_j) and jet diameter (D_j). The signals are collected at the same spatial location indicated by the black diamond symbol. Here, the vertical dash line represents $St_j = 0.93$.

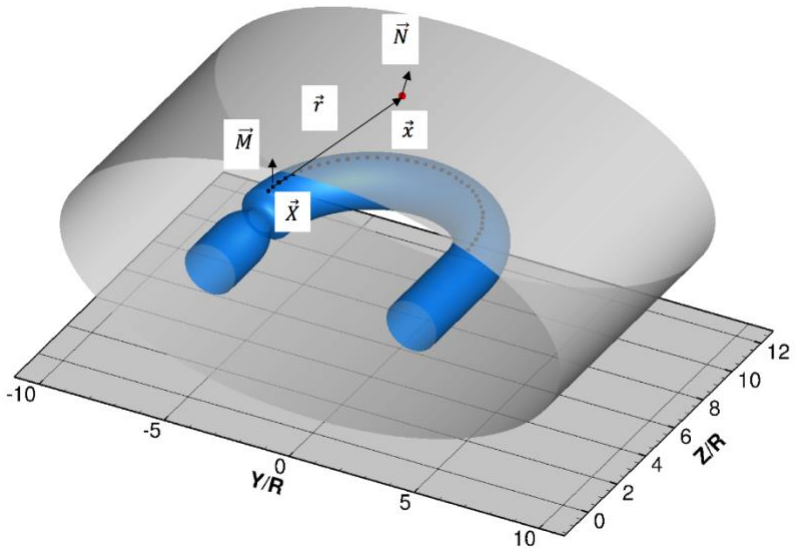

Fig. 13 Illustration of the forward problem using the free-space Green's function. The black squares are the point sources located on the aortic wall, and the red circle represents the target point on the epidermal surface of the thorax.

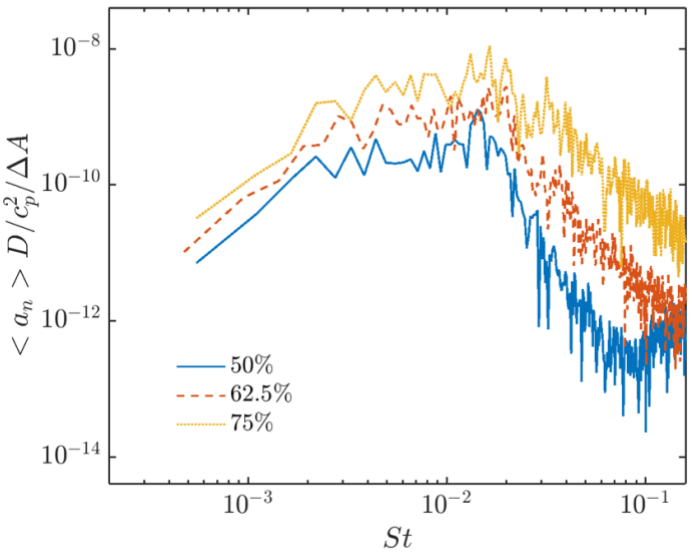

Fig. 14 Spectra of the wall-normal acceleration calculated from the free-space Green's function. The location at which these signals are calculated and the scaling of the Strouhal number are the same as Fig. 11.

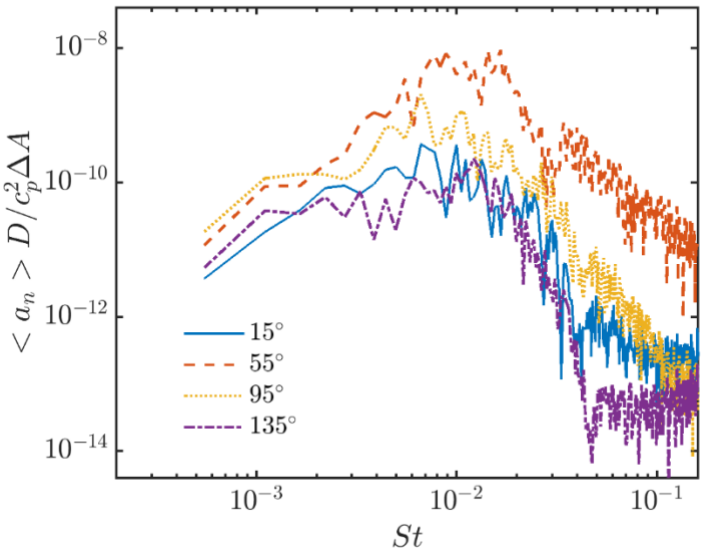

Fig. 15 Spectra calculated from individual point source (black squares in Fig. 13) at selected angle θ for 75% case. The location at which these signals are calculated and the scaling of the Strouhal number are the same as Fig. 11.

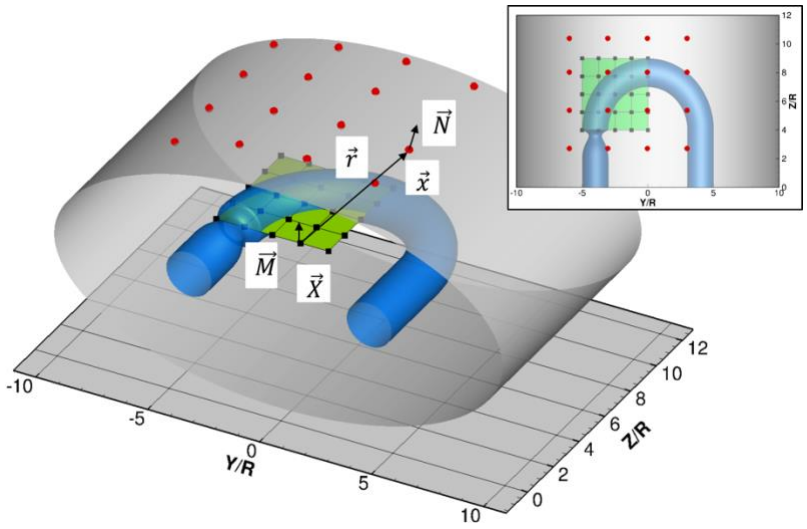

Fig. 16 Illustration for the source localization problem using free-space Green's function. The green patch is the plane where source location is evaluated, and it is discretized into a 5×5 grid. The red circles on the skin surface represent the 4×4 sensor array.

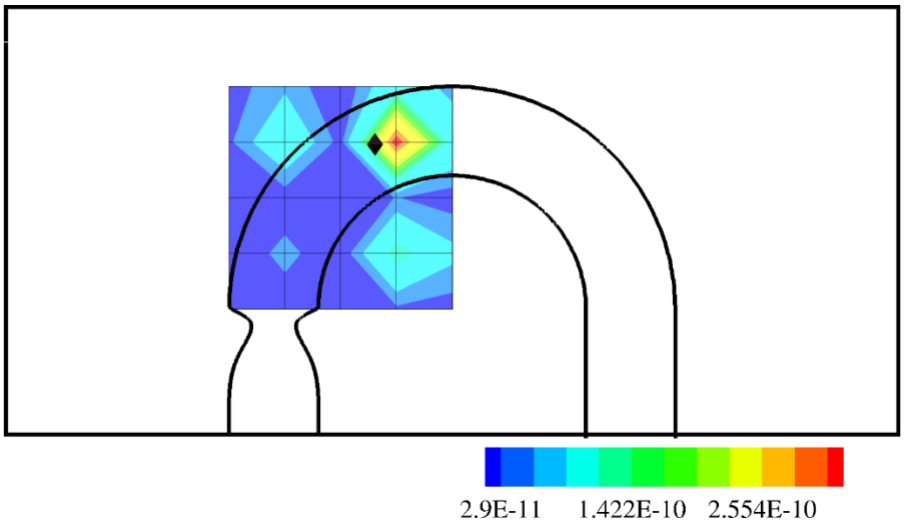

Fig. 17 Source localization using free-space Green's function for 75% case on the green patch shown in Fig. 16. The black diamond symbol represents the same spatial location as in Fig. 9a.